Research Square

Preprints are preliminary reports that have not undergone peer review.
They should not be considered conclusive, used to inform clinical practice,
or referenced by the media as validated information.

Optimization of Laser Ablation Resistance for Multilayer Heterogeneous Thin Films Based on Optical–Thermal–Ablation Coupling and a BP Neural Network Surrogate Model

Yuyang Shen
Yangzhou University
Shu Zheng
zhengshu@yzu.edu.cn
Yangzhou University
Duanpeng He
China Aerospace Components Engineering Center
Yang Cui
Yangzhou University
Yan Li
China Aerospace Components Engineering Center
Yuxiong Xue
Yangzhou University

Research Article

Keywords: Multilayer thin films, Laser heating, Phase change, Optical-thermal coupling, Neural network surrogate, Thermal optimization

Posted Date: November 11th, 2026

DOI: https://doi.org/10.21203/rs.3.rs-11533304/v1

License: This work is licensed under a Creative Commons Attribution 4.0 International License.
Read Full License

Additional Declarations: No competing interests reported.

Optimization of Laser Ablation Resistance for Multilayer Heterogeneous Thin Films Based on Optical–Thermal–Ablation Coupling and a BP Neural Network Surrogate Model

Yuyang Shen[a], Shu Zheng[a,*], Duanpeng He[b], Yang Cui[a], Yan Li[b], Yuxiong Xue[a,*]
[a] *College of Electrical, Energy and Power Engineering, Yangzhou University, Yangzhou, 225127, China*
[b] *China Aerospace Components Engineering Center, Beijing, 100094, China*

Abstract: The thermophysical response of multilayer heterogeneous thin films under continuous-wave laser heating involves non-uniform volumetric heat generation modulated by interference-induced standing-wave absorption, which governs the layer-by-layer phase-change sequence and the ultimate thermal failure threshold—a coupling that conventional Beer–Lambert approximations fail to capture. This study develops an optical–thermal–ablation coupled model that resolves the standing-wave absorption profile and couples it to temperature-dependent transient heat conduction with latent-heat effects, validated against laser-damage experiments at seven power levels. A two-stage surrogate-based framework is constructed to explore the thermophysical design space in which discrete material choices and continuous layer thicknesses jointly control the absorption distribution and melting sequence. The optimal architecture is identified as SUS304/Ag/Si_3N_4/SiO_2/ITO with a refined thickness profile of 21 μm/0.106 μm/0.18 μm/2.35 μm/0.05 μm under a 25 μm total constraint, yielding a 209.6 K reduction in peak temperature relative to the baseline. The analysis reveals three thermophysical mechanisms: (i) in the interference layer, the order-of-magnitude reduction in volumetric optical absorption dominates over the 2.5-fold difference in thermal conductivity in determining the peak temperature; (ii) the positive temperature coefficient of thermal conductivity in the SUS304 substrate provides a self-regulating thermal-sink effect; and (iii) the Ag layer exhibits a non-monotonic thermal response beyond its optical saturation thickness, governed by the competition between cross-plane thermal resistance and in-plane thermal spreading coupled with absorption-peak shifting. These results clarify how interference-modulated heat generation governs phase-change sequences and thermal failure in multilayer thin films.

Keywords: Multilayer thin films; Laser heating; Phase change; Optical-thermal coupling; Neural network surrogate; Thermal optimization

1. Introduction

High-power continuous-wave (CW) lasers, owing to their stable power output and excellent beam quality, have seen extensive application in industrial manufacturing—such as laser cutting, welding, and surface treatment—and their usage is expanding into critical components of high-power laser equipment and precision optoelectronic systems[1-2]. In these systems, multilayer thin-film structures including anti-reflection coatings, high-reflection mirrors, beam splitters, and transparent conductive films are

* Corresponding authors.
E-mail addresses: zhengshu@yzu.edu.cn (S. Zheng), yxxue@yzu.edu.cn (Y. Xue).

essential for tailoring optical field propagation, achieving target spectral responses, and enhancing overall optical performance. However, under off-normal operating conditions, such as beam misalignment or accidental direct illumination on optical windows, these thin-film components can be subjected to thermal loads far exceeding their design thresholds within milliseconds[3]. Such extreme thermal exposure causes irreversible structural damage and failure of the multilayer films, ultimately compromising the operational safety of the entire laser system.

Research into the thermal damage responses of multilayer thin-film structures under laser irradiation remains an active and evolving field. On the experimental front, Taylor et al.[4] evaluated the damage thresholds of HfO_2/SiO_2 homogeneous versus nanolaminate films under continuous-wave laser irradiation, revealing that nanolaminate structures exhibit lower damage resistance. Xu et al.[5] demonstrated that the damage morphology of multilayer dielectric gratings evolves systematically with increasing CW laser power. Similarly, Kim et al.[6] conducted optical characterization and finite-element thermal analysis on HfO_2/SiO_2 multilayer diffraction gratings under CW laser exposure, providing order-of-magnitude estimates for laser damage thresholds. However, these investigations predominantly focused on pulsed laser regimes or conventional all-dielectric systems; experimental and quantitative insights into heat accumulation and layer-by-layer failure in heterogeneous thin films containing metal and transparent conductive layers under CW irradiation remain remarkably scarce. Regarding numerical modeling, Zhang et al.[7] proposed a one-dimensional Green's function framework to evaluate the photothermal response of complex multilayer systems, validating it against finite element method (FEM) simulations; however, their focus was restricted to forward temperature calculations rather than inverse optimization or quantitative melting failure analysis. Bovard and Macleod[9] iteratively coupled characteristic-matrix optical calculations with heat conduction equations to simulate photothermal nonlinear dynamics under intense irradiation[8]. Moorhead and Avedisian established a photothermal deflection model for multilayer films under modulated laser heating, yet without integrating wave-optical interference or phase-change phenomena. Grigoriev et al.[10] developed an efficient numerical approach for optical multilayer heating, but their model was tailored strictly to all-dielectric systems, failing to capture heterogeneous layer-by-layer melting dynamics. Furthermore, Yamada[11] modeled thermal transport during semiconductor annealing under scanning CW lasers, while Braun and Hopkins[12] defined theoretical upper-bound limits for thermal penetration depth in multilayer films. In specific energy applications, Ahmmed and Huda[13] simulated conjugate heat transfer in the CZTS/Mo/glass solar-cell absorber under continuous-wave laser irradiation using OpenFOAM, and Zhang et al. [14] analyzed the thermal response of a SiO_2/Ge/sapphire three-layer structure under an 808 nm CW laser using a coupled FDTD-FEM method. In parallel, photothermal deflection techniques were introduced by Gallais and Commandré for absorption characterization[15]. As highlighted by Ocak et al.[16] from a heat transfer perspective, the optical architecture of multilayer films intrinsically dictates electric-field and temperature distributions, underscoring the strong and non-negligible coupling between optical field interference and thermal response.

Regarding the numerical modeling of laser-induced melting and phase-change phenomena, Voller and Prakash[17] pioneered the fixed-grid enthalpy method, Nedjar[18] developed an enthalpy-based finite element formulation, and Kopp et al. [19] implemented the apparent heat capacity approach to model phase transitions in laser powder bed fusion. Brent et al. [20] extended the enthalpy-porosity technique to account for convection within the mushy zone. Resl et al. [21] proposed a numerical framework for phase-change phenomena in thin films validated by experimental analysis, however, their model was restricted to single-layer configurations and failed to address the progressive layer-by-layer melting dynamics of multilayer stacks. He and Zhigilei[22] employed a multiscale modeling approach to simulate short-pulse laser-induced melting, resolidification, and amorphization in silicon, systematically characterizing the temperature-dependent velocities of the melting and crystallization fronts.

For the structural design of ablation-resistant multilayer thin films, conventional optimization approaches heavily rely on single-variable parametric sweeps or brute-force finite element scans. Given the high-dimensional design space inherently associated with multilayer configurations, traditional numerical algorithms are computationally prohibitive and highly susceptible to local minima. In recent years, surrogate modeling techniques—particularly deep neural networks—have emerged as powerful tools to dramatically accelerate structural optimization. For example, Malkiel et al.[23] applied deep learning to the design and characterization of plasmonic nanostructures targeting tailored optical responses. Peurifoy et al.[24] implemented neural networks for the inverse design of multilayer nanophotonic structures with continuous geometric parameters. Alkhazraji et al.[25] coupled a fully connected neural network surrogate model with the Non-dominated Sorting Genetic Algorithm II (NSGA-II) algorithm[26], achieving rapid spectral predictions and multi-objective optimization for multilayer Ta_2O_5/MgF_2 thin films. Unni et al.[27] proposed a tandem optimization framework based on a mixture density network for the on-demand inverse design of high-reflection coatings; this architecture effectively resolved the non-uniqueness challenge inherent in inverse problems, accurately reconstructing reflection spectra for up to 20-layer thin-film architectures.

In summary, current research in this domain exhibits several key limitations. First, most existing models rely on the simplified Beer-Lambert exponential decay or boundary heat flux assumptions rather than rigorously solving the Helmholtz wave equation for standing-wave absorption distributions; consequently, they fail to capture the intrinsic coupling between intra-layer absorption peaks and the progressive layer-by-layer melting sequence. Second, existing literature predominantly focuses on all-dielectric thin-film systems targeting tailored optical performance, with little emphasis on thermal-protection-oriented designs for heterogeneous stacks integrating metals, ceramics, and oxides. Third, at the structural optimization level, traditional approaches rely heavily on empirical trial-and-error or single-factor parameter sweeps; global optimization within high-dimensional hybrid discrete-continuous design spaces (encompassing material stacking sequences and layer thicknesses) remains rarely explored. Finally, experimental laser damage characterization of multilayer heterogeneous coatings is cost-prohibitive, while in situ temperature diagnostics within

sub-micron film layers present formidable technical challenges. Therefore, developing robust numerical models capable of capturing coupled optical–thermal–phase-change dynamics is imperatively needed to complement and guide experimental exploration.

To address the above issues, this study combines finite element simulations with a neural network surrogate model to propose an ablation-resistant optimization design methodology, systematically optimizing both material selection and layer thicknesses for multilayer heterogeneous thin films. First, a coupled numerical model combining Helmholtz wave optics and transient heat conduction is established, in which the apparent heat capacity method is introduced to describe the endothermic phase-transition behavior of each layer near its melting point. The coupled model and phase-change dynamics are numerically solved using the finite element method. Taking the melting point of the substrate as the ablation failure criterion, this study cross-validates the critical laser power predicted by simulation against experimentally observed ablation damage data. Second, a Back-Propagation (BP) neural network surrogate model is trained on the validated simulation dataset, taking the maximum film temperature at a specific irradiation time as the core optimization objective to perform a global search for the optimal thin-film structure. Finally, the candidate structures optimized by the neural network are fed back into the finite element model for closed-loop verification. This study provides technical support for the ablation-resistant structural design of multifunctional thin films under continuous-wave laser environments.

2.Construction of the Optical-Thermal-Ablation Coupled Model

2.1 Multilayer Heterogeneous Thin-Film Structure

The geometric configuration and initial layer thicknesses of the multilayer heterogeneous thin-film structure investigated in this study are shown in Fig. 1. The initial architecture comprises five functional layers: an antistatic transparent conductive top layer, a thermal buffering and optical tuning layer, an optical interference control layer, a metallic reflective layer, and a rigid metallic substrate. Specifically, the top transparent conductive layer combines infrared transmittance with electrical conductivity, permitting laser transmission into the film stack while providing anti-static functionality. The underlying thermal buffering and optical tuning layer, together with the optical interference control layer, are composed of dielectric materials with low thermal conductivities and high melting points, serving to insulate heat, buffer thermal transport, and tailor internal electromagnetic field distributions. The metallic reflective layer serves to reflect the incident laser beam. Finally, the metallic substrate provides structural support while acting as a heat sink for the reflective layer.

The initial thicknesses of the respective layers are 0.02 μm for the antistatic layer, 2.6 μm for the thermal buffering and optical tuning layer, 0.15 μm for the optical interference layer, 0.15 μm for the metallic reflective layer, and 20.5 μm for the metallic substrate. The total thickness of the five-layer stack is subject to a design constraint not exceeding 25 μm.

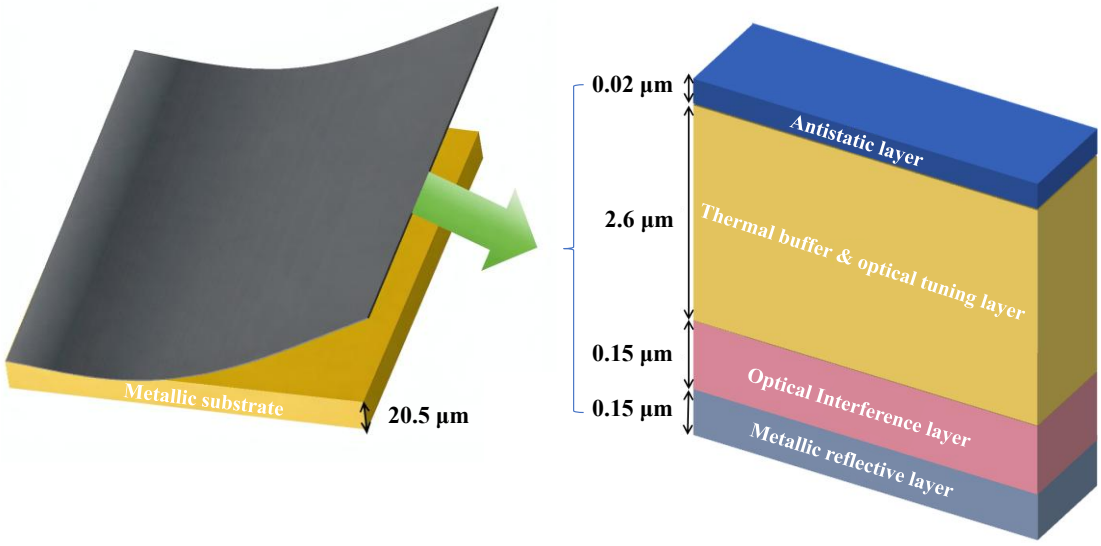


Fig. 1 Schematic of the multilayer heterogeneous thin-film structure

A finite element geometric model of the initial thin-film structure is established and discretized using a structured mesh. A mapped mesh scheme is applied along the thickness direction to ensure that each layer contained multiple elements capable of resolving spatial variations in the electromagnetic field. In the mesh transition region, node coupling is implemented to ensure physical field continuity across interfaces. To verify mesh convergence, the peak film temperature is evaluated under a laser power of 115 W and an irradiation duration of 1.3 s using three mesh configurations with maximum element sizes of 1 μm, 0.5 μm, and 0.3 μm. As shown in Fig. 2, the calculated peak temperatures for the three mesh schemes are 1718.3 K, 1746 K, and 1747 K, respectively. The temperature deviation between the 0.5 μm and 0.3 μm mesh configurations is less than 1%, demonstrating that a maximum element size of 0.5 μm fully satisfies the required numerical accuracy. Balancing computational expense and solution efficiency, a mapped mesh with a maximum element size of 0.5 μm and a minimum element size of 0.01 μm is adopted for all subsequent simulations in this study.

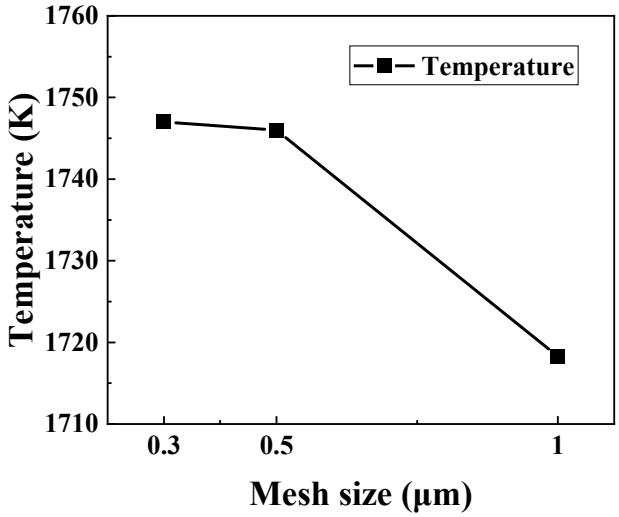


Fig. 2 Mesh convergence

2.2 Optical Theory

The energy distribution of the laser in the multilayer thin-film structure is governed by the frequency-domain Helmholtz equation:

$$\nabla \times (\nabla \times \mathbf{E}) - k_0^2 \varepsilon_r \mathbf{E} = 0 \tag{1}$$

$$k_0 = \frac{2\pi}{\lambda} \tag{2}$$

$$\varepsilon_r = (n - ik)^2 \tag{3}$$

where, $\mathbf{E}$ is the electric field intensity vector, k_0 is the vacuum wavenumber, λ is the incident laser wavelength, ε_r is the relative permittivity, and n and k are the refractive index and extinction coefficient of the material, respectively.

In the multilayer thin-film structure, the tangential components of the electric and magnetic fields at the interface between adjacent layers satisfy the continuity conditions:

$$\mathbf{n} \times (\mathbf{E}_i - \mathbf{E}_{i+1}) = 0, \quad \mathbf{n} \times (\mathbf{H}_i - \mathbf{H}_{i+1}) = 0 \tag{4}$$

where **n** is the unit normal vector to the interface, and **H** is the magnetic field strength.

The incident laser is modeled as a plane wave at normal incidence propagating along the *z* direction, with the polarization direction along the *x* axis. The peak power density of the incident laser is:

$$I_0 = \frac{2P}{\pi \omega_0^2} \tag{5}$$

where P represents the laser power and ω_0 is the spot radius. The corresponding electric field amplitude E_0 is expressed as:

$$E_0 = \sqrt{\frac{2I_0}{c\varepsilon_0}} \tag{6}$$

where c is the speed of light and ε_0 is the vacuum permittivity. At the upper boundary of the computational domain, $z = 0$ (the laser incidence surface), the incident electric field is specified and an absorbing boundary condition is applied to suppress non-physical reflections:

$$\mathbf{n} \times (\nabla \times \mathbf{E}) - ik_0(\mathbf{n} \times \mathbf{E} \times \mathbf{n}) = 2ik_0 \mathbf{E}_{inc} \tag{7}$$

where $\mathbf{E}_{inc}$ is the incident electric field vector, with amplitude E_0.

The side and bottom boundaries are truncation boundaries, with no incident wave entering; homogeneous absorbing boundary conditions are imposed to eliminate spurious reflections:

$$\mathbf{n} \times (\nabla \times \mathbf{E}) - ik_0(\mathbf{n} \times \mathbf{E} \times \mathbf{n}) = \mathbf{0} \tag{8}$$

Optical absorption at layer interfaces can significantly alter the temperature field distribution inside the multilayer film, with heat generated by interfacial absorption accounting for a substantial fraction of total energy deposition[28]. Therefore, this model rigorously enforces field continuity conditions across all internal interfaces to accurately capture electromagnetic loss. From the electric field distribution obtained by solving the optical governing equations, the resistive loss power density Q_e is calculated as:

$$Q_e = \frac{1}{2}\varepsilon_0 \varepsilon_r'' \omega |\mathbf{E}|^2 \tag{9}$$

$$\omega = \frac{2\pi c}{\lambda} \tag{10}$$

where ε_r'' is the imaginary part of the relative permittivity, and ω is the angular frequency of the laser.

2.3 Heat Conduction Theory

The spatio-temporal evolution of the temperature field within the thin-film structure is governed by the transient Fourier heat conduction equation:

$$\rho C_p \frac{\partial T}{\partial t} = \nabla \cdot (k \nabla T) + Q \tag{11}$$

where ρ is the material density, C_p is the specific heat capacity, T is the temperature, k is the thermal conductivity, and Q is the volumetric heat source term. Here, Q equals the electromagnetic resistive loss power density (Q_e) computed by the wave optics module, thereby establishing the forward coupling between the electromagnetic field and the temperature field.

At the internal horizontal interfaces between adjacent layers (extending along the x-direction), temperature and normal heat flux satisfy the continuous boundary conditions:

$$T_i = T_{i+1}, k_i \frac{\partial T_i}{\partial y} = k_{i+1} \frac{\partial T_{i+1}}{\partial y} \tag{12}$$

At the initial time $t = 0$, the entire thin-film system is in thermal equilibrium with the ambient temperature T_0:

$$T(x, y, 0) = T_0 \tag{13}$$

The top surface (y=0, laser-irradiated surface) undergoes combined convective and radiative heat exchanges with the ambient environment:

$$-k \frac{\partial T}{\partial y}|_{y=0} = q_{\text{conv}} + q_{\text{rad}} \tag{14}$$

$$q_{\text{conv}} = h(T - T_0) \tag{15}$$

$$q_{\text{rad}} = \varepsilon_{\text{rad}} \sigma (T^4 - T_0^4) \tag{16}$$

where h is the convective heat transfer coefficient, ε_{rad} is the surface thermal emissivity, and σ is the Stefan–Boltzmann constant.

The bottom and lateral boundaries are specified as adiabatic (insulated) conditions:

$$\frac{\partial T}{\partial n} = 0 \tag{17}$$

2.4 Effective Heat Capacity Method for the Ablation Process

When the material in each layer reaches its melting point during heating, a solid–liquid phase transition occurs, accompanied by the absorption or release of latent heat. In this study, the apparent heat capacity method is adopted to model this phase-change process. By modifying the specific heat capacity within the phase-change temperature interval, the latent heat contribution is implicitly incorporated, bypassing explicit

tracking of the moving phase-change interface. The thermophysical properties of the material within the phase-change interval are defined in terms of solid and liquid phases, with each property parameter calculated using a volume-fraction-weighted average.

The density is determined by the volume-fraction-weighted average of the solid and liquid phases:

$$\rho = \theta_1 \rho_1 + \theta_2 \rho_2 \tag{18}$$

where θ_1 and θ_2 are the volume fractions of the solid and liquid phases, respectively, satisfying $\theta_1+\theta_2=1$.

The specific heat capacity encompasses both the sensible heat contribution and the latent heat contribution within the phase-change interval:

$$C_p = \theta_1 C_{p,1} + \theta_2 C_{p,2} + L\frac{\partial \alpha_m}{\partial T} \tag{19}$$

where L is the latent heat of phase change per unit mass, and α_m is the liquid mass fraction. $\frac{\partial \alpha_m}{\partial T}$ is approximated by a smooth step function within the phase-change temperature interval, which distributes the latent heat continuously over the transition window and prevents numerical singularities.

The liquid mass fraction α_m is defined as a continuously differentiable function of temperature:

$$\alpha_m = f(T) \tag{20}$$

The thermal conductivity is also calculated by a volume-fraction-weighted average:

$$k = \theta_1 k_1 + \theta_2 k_2 \tag{21}$$

The latent heat contribution term is non-zero only within the phase-change temperature window. The transition interval is set to 5 K; an excessively narrow temperature interval may cause numerical non-convergence.

The thermophysical phase-transition parameters, including the melting points and latent heats of phase change for the respective functional layers, are incorporated into the apparent heat capacity model. Each layer independently evaluates whether its melting temperature has been reached, triggering phase transitions on a layer-by-layer basis. This sequential melting dynamics is intimately linked to the spatial distribution of standing-wave absorption peaks within the film stack. If a high absorption peak coincides with a layer possessing a lower melting point, that layer undergoes preferential melting. The rigid metallic substrate serves as the ultimate barrier against thermal ablation; prior to its melting, even if localized phase transitions occur within the upper layers, the structural integrity and protective capability of the overall film stack remain preserved. Once the substrate undergoes melting, the entire architecture suffers irreversible failure, forfeiting its load-bearing capacity and thermal protection. Consequently, the onset of substrate melting is established as the critical criterion for ablation failure.

2.5 Model Validation

To verify the accuracy of the established optical–thermal–ablation coupled model,

a comparative validation study is conducted between continuous-wave laser irradiation experiments and numerical simulations. The experimental sample is a custom-designed five-layer thin-film architecture. From the top incident surface to the substrate, the stack sequentially comprises an antistatic layer, a thermal buffering and optical tuning layer, an optical interference layer, a metallic reflective layer, and the metallic substrate, with structural parameters identical to those described in Section 2.1. The optical and thermophysical properties of the functional layers in the multilayer film stack are shown in Table 1.

Table 1 Optical and thermophysical properties of the functional layers in the multilayer film stack

Functional layer	Refractive index n (1064 nm)	Extinction coefficient k (1064 nm)	Melting temperature (K)	Latent heat of phase change L (kJ/kg)
Metallic substrate	3.8298	5.3354	1723	247
Metallic reflective layer	0.0516	3.9046	1234	105
Optical interference layer	1.6171	0.0001	2328	1137.9
Thermal buffering and optical tuning layer	1.4588	0.0009783	1999	148
Antistatic layer	1.7153	0.0209	2183	-

The fabricated prototype sample is shown in Fig. 3(a). The incident laser spot radius was set to 3 mm, and the ambient temperature is maintained at 293.15 K, matching the numerical simulation configurations. Figs. 3(b) and 3(c) display the front and back surfaces of the sample following exposure to a 30 W laser beam. Here, the front side corresponds to the antistatic layer, and the back side corresponds to the metallic substrate.

Under laser irradiation, no macroscopic morphological damage is observed on the front surface, whereas a distinct circular thermal spot emerges on the rear surface of the substrate. This phenomenon indicates that longitudinal heat conduction within the film stack has fully developed toward the substrate side, while the temperature at the incident interface remains below its visible damage threshold. Although each functional layer in the film stack exhibits slight optical absorption, the extinction coefficient of the metallic reflective layer at 1064 nm is substantially higher than other layers. Consequently, heat generated within the metallic reflective layer—acting as the primary absorption layer—is preferentially conducted toward the metallic substrate along the path of minimal thermal resistance, forming an efficient downward heat dissipation channel. Concurrently, the thermal buffering and optical tuning layer provides upward thermal resistance, slightly hindering heat transfer toward the top surface. As a result, the temperature rise on the back of the substrate reaches the observable threshold earlier than that on the irradiated surface, reflecting the thermal management features of the film stack wherein downward heat dissipation dominates and upward thermal insulation provides protection.

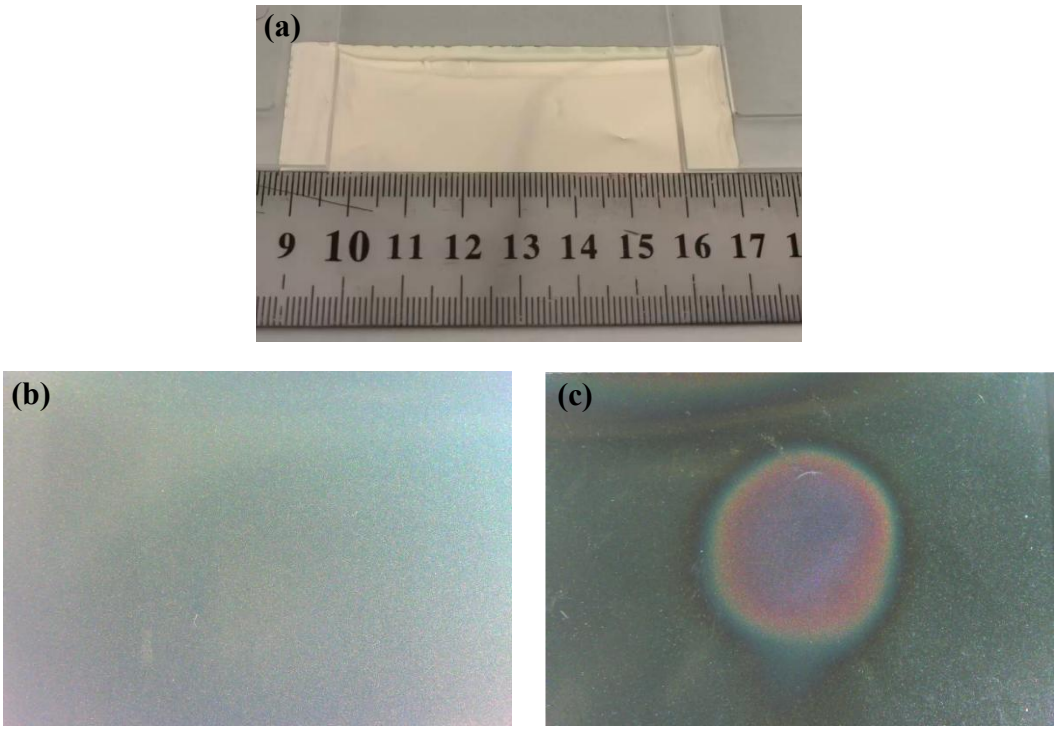


Fig. 3 Samples before and after 30 W laser irradiation: (a) initial sample before irradiation; (b) front view (antistatic layer side) after 30 W irradiation; (c) back view (substrate side) after 30 W irradiation.

Fig. 4 illustrates the simulated layer-by-layer ablation evolution within the five-layer thin-film structure. In Figs. 4(a) and 4(c), the contour value 0 denotes unablated solid material, 1 represents fully melted liquid material, and intermediate values characterize the solid-liquid phase-change transition. At t=0.4 s, the metallic reflective layer possessing the highest extinction coefficient undergoes preferential melting, while the remaining layers remained structurally intact, as shown in Fig. 4(b). By t=1.4 s, heat conducted through the stack caused the metallic substrate temperature to exceed its critical melting threshold, as shown in Fig. 4(d), triggering structural melting failure of the substrate. This sequentially triggers ablation trend closely matches the experimental observations. Furthermore, Fig. 4(e) illustrates the global ablation profile of the complete film stack at t=1.4 s. It can be clearly observed that structural ablation failure is highly localized within the central laser-irradiated domain, confirming the spatial boundary character of the laser-induced thermal load.

Validation across a broader operational range is subsequently performed using seven distinct laser power levels, as detailed in Table 2. Across all test cases, the damage states predicted by the coupled model are in complete agreement with the experimental findings. For the first three power levels (30–50 W), no ablation damage is observed experimentally, and the simulated peak temperatures remained below the substrate melting threshold. For the remaining four higher-power groups (55–115 W), ablation failure occurs within the corresponding exposure times, with simulated damage profiles matching the experimental observations. These comparisons demonstrate that the established coupled model accurately predicts the thermal evolution and ablation behavior of multilayer thin-film architectures under continuous-wave laser irradiation.

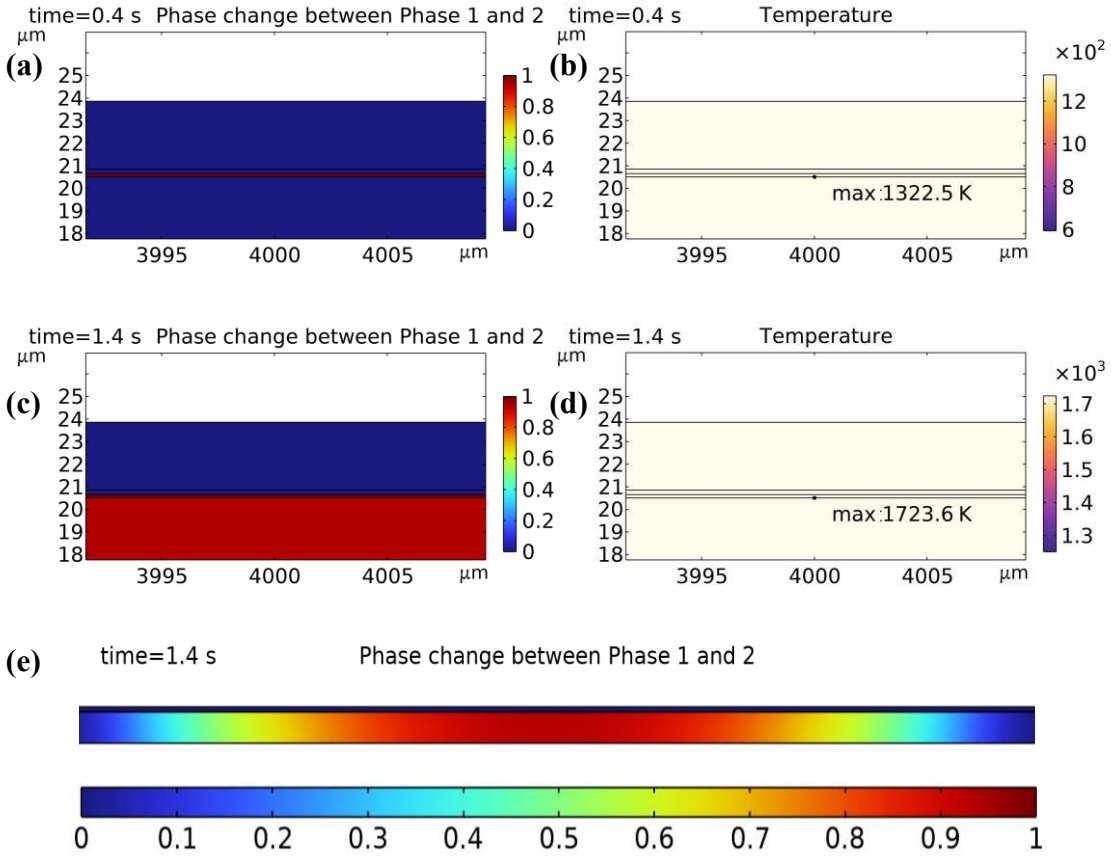


Fig. 4 Simulated ablation and temperature distributions of the multilayer thin-film structure: (a) localized ablation state of the metallic reflective layer at 0.4 s; (b) localized temperature field of the metallic reflective layer at 0.4 s; (c) localized ablation state of the metallic substrate at 1.4 s; (d) localized temperature field of the metallic substrate at 1.4 s; (e) global ablation contour across the entire film stack at 1.4 s

Table 2 Comparison of experimental and simulation conditions and results.

Laser power (W)	Power density at target (W/cm^2)	Irradiation time (s)	Experimental phenomena	Simulation results
30	106.1	120	No damage	No damage
40	142.1	120	No damage	No damage
50	177.1	120	No damage	No damage
55	193.8	3.4	Damage	Damage
80	282.5	1.6	Damage	Damage
100	352.2	1.4	Damage	Damage
115	405.9	1.3	Damage	Damage

3. Structural Optimization Based on a BP Neural Network Surrogate Model

Although the optical–thermal–ablation coupled finite element model can accurately predict the transient thermal response of a specified film architecture, each full-field simulation is computationally intensive and impractical for high-frequency call routines during numerical optimization iterations. The essence of laser anti-ablation structural design for multilayer films lies in the collaborative configuration across two distinct dimensions: material selection (which determines optical absorption and

reflection) and functional layer thickness (which governs standing-wave phase distributions and thermal conduction pathways). The inherent mixed-discrete-continuous nature of these decision variables presents substantial computational challenges for high-dimensional search algorithms. To address this issue, this study proposes a two-stage decoupled global optimization framework leveraging a BP Neural Network surrogate model. This strategy systematically decomposes the mixed-variable optimization into two sequential subproblems: discrete material candidate screening and continuous layer-thickness optimization. The detailed optimization workflow is illustrated in Fig. 5.

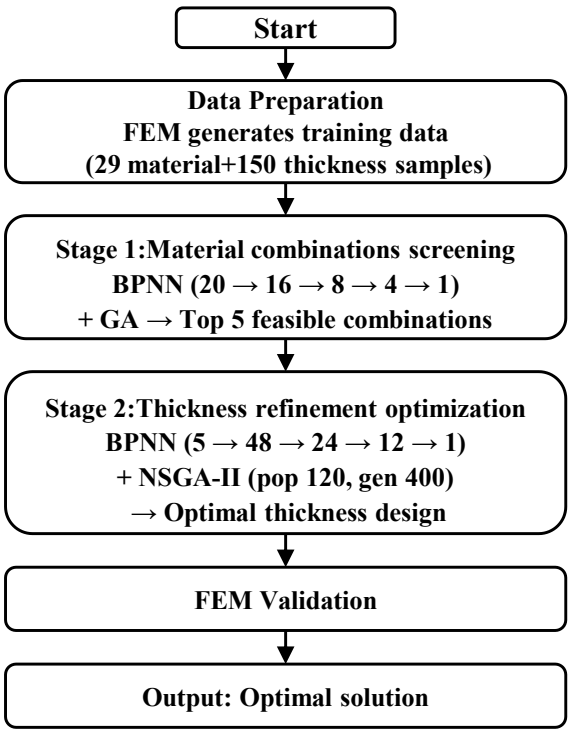


Fig. 5 Neural network optimization workflow

Stage 1: Discrete material combination screening. The thickness of each functional layer is initially fixed at its baseline value, thereby decoupling material combination screening from thickness optimization. Consequently, the optimization in this stage is confined to the discrete variable space, eliminating coupling perturbations from continuous thickness variations. A BP neural network is constructed to establish a high-efficiency surrogate mapping from material combinations to peak transient temperatures, replacing the computationally expensive finite element simulations as the objective evaluation function within the Genetic Algorithm (GA) framework.

Stage 2: Continuous thickness optimization. Once the optimal material candidate combination is identified and fixed, the structural refinement transitions into the continuous parameter space. Unlike discrete material selection, the thermal response exhibits complex, highly non-monotonic dependencies on layer thickness variations. This multivariable, nonlinearly coupled behavior necessitates a global exploration algorithm capable of avoiding local gradient minima. In this stage, a BP neural network is trained to construct a precise surrogate mapping between functional layer thicknesses and the peak temperature response. Subsequently, 150 sample points generated via

Latin Hypercube Sampling (LHS) are utilized to span the five-dimensional thickness design space, upon which the NSGA-II algorithm performs multi-objective global optimization.

3.1 Material Screening

3.1.1 Dataset and Surrogate Model Structure

Candidate materials are chosen based on their intended functional roles across the film stack, encompassing 15 candidate materials in total, as listed in Table 3. Note that for the thermal buffering and optical tuning layer, no alternative candidate material satisfied the strict application constraints; hence, its material selection remained fixed. The dataset for the stage 1 material screening is generated using the optical–thermal–ablation coupled finite element model, yielding 29 distinct material combination samples. Each sample represents a unique five-layer material configuration, with the thickness of each functional layer initially set to its baseline value.

Table 3 List of candidate materials

Functional layer	Candidate materials	Number of candidates
Metallic substrate	SUS304、TC4、Invar alloy	3
Metallic reflective layer	Au、Ag、Al	3
Optical interference layer	Y_2O_3、Al_2O_3、AlON、Si_3N_4、MgO	5
Thermal buffering and optical tuning layer	SiO_2	1
Antistatic layer	AZO、ITO、TTO	3

The input feature vector integrates both the categorical material designations and layer thickness parameters. Categorical material variables are mapped via layer-wise one-hot encoding. With the number of candidates for Layers 1 through 5 being 3, 3, 5, 1, and 3, respectively, the material encoding yields a 15-dimensional discrete feature vector. Concatenating this with the 5 continuous layer-thickness variables constructs a 20-dimensional input feature space for the surrogate model.

The material screening surrogate model adopts a multilayer feedforward neural network architecture incorporating three hidden layers. The input layer accommodates a 20-dimensional feature vector, followed by three hidden layers comprising 16, 8, and 4 neurons, respectively, with a 1-dimensional output layer predicting the peak transient temperature. The topology is illustrated in Fig. 6. This architecture follows a pyramidal layer-by-layer dimensionality reduction strategy: the first hidden layer (16 neurons) extracts initial low-level feature representations from the 20-dimensional input; the second hidden layer (8 neurons) performs feature interaction and synthesis; and the third hidden layer (4 neurons) further abstracts these into core latent representations. All hidden layers employ the Rectified Linear Unit (ReLU) activation function. To mitigate overfitting, Batch Normalization (BN) and Dropout (with a dropout rate of 0.3) are incorporated into the first two hidden layers.

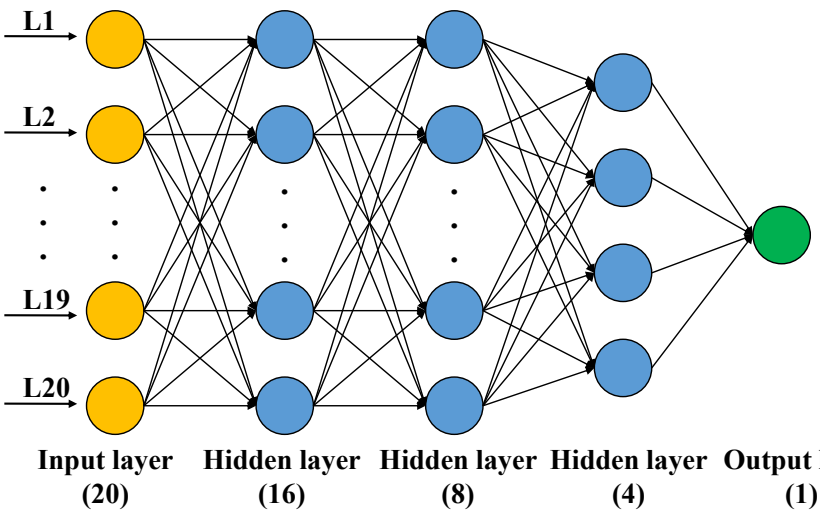


Fig. 6 Network architecture of the BP neural network surrogate model for material screening

To guarantee strict reproducibility of the computational results, all stochastic processes—including neural network weight initialization, dataset partitioning, and the generation of initial populations and mutation operations in the Genetic Algorithm (GA)—are governed using a fixed random seed.

3.1.2 Model Training and Genetic Algorithm Search

The network training is executed using the Adam optimizer with an initial learning rate of 5×10^{-4}, a weight decay coefficient of 10^{-4}, and a maximum training budget of 600 epochs. A dynamic learning rate scheduler reduces the learning rate by 50% if the validation loss fails to decrease within 50 consecutive epochs. The dataset (29 samples in total) is randomly partitioned into training and validation sets at an 8:2 ratio, yielding 23 samples for training and 6 samples for validation.

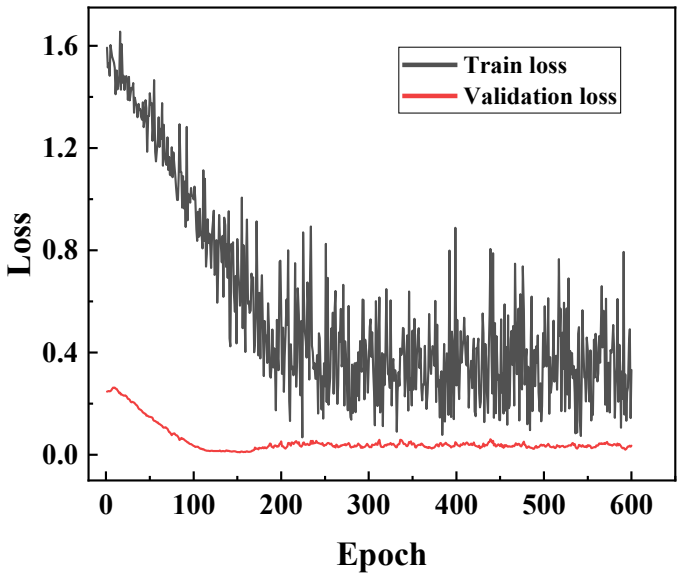


Fig. 7 Training and validation loss curves of the material screening surrogate model

The corresponding training and validation loss curves are illustrated in Fig. 7. The training loss exhibits moderate fluctuations, primarily originating from stochastic

gradient noise inherent to the small-sample regime (23 training samples). The validation loss decreases smoothly, demonstrating that the model achieves stable overall convergence without overfitting.

Utilizing the trained BP neural network surrogate model, a GA is deployed to conduct a global search for optimal material candidate combinations. The primary optimization objective is to minimize the predicted peak transient temperature:

$$\min_{\mathbf{M}} T_{peak} = f_{BP}(\mathbf{M}) \tag{22}$$

where $\mathbf{M} = (M_1, M_2, M_3, M_4, M_5)^T$ represents the discrete candidate material vector across the five functional layers. A thermal reliability constraint is incorporated: the local temperature of the metallic substrate must remain strictly below the melting point of the candidate substrate material, which is dynamically enforced via the fitness evaluation function. The GA configuration comprises a population size of 50, a maximum generation limit of 80, a crossover probability of 0.8, and a mutation probability of 0.3. A tournament selection scheme with a tournament size of 3 is implemented for selection. Upon termination of the algorithm, the top five feasible material candidate combinations are exported to serve as candidate schemes for the subsequent second-stage thickness optimization. These optimal combinations will be comprehensively evaluated in Section 4.

3.2 Thickness Optimization

3.2.1 Dataset and Surrogate Model Structure

The dataset for the stage 2 thickness optimization comprises 150 samples generated using the optical–thermal–ablation finite element model. Holding the optimal material combination identified in Stage 1 constant, Latin hypercube sampling[29] is performed over the five-dimensional layer thickness space within their designated feasible ranges. These sampling points are evaluated sequentially in the finite element framework to compute the corresponding peak transient temperatures, thereby constructing the thickness–temperature mapping dataset. The input feature vector consists of the five continuous layer thickness parameters (5 dimensions):

$$\mathbf{L} = (L_1, L_2, L_3, L_4, L_5)^T \tag{23}$$

The target output is the peak transient temperature T_{peak}. The admissible design intervals for each layer thickness are detailed in Table 4.

Table 4 Admissible thickness design intervals for each functional layer

Layer designation	Functional layer	Minimum thickness (μm)	Maximum thickness (μm)
L1	Metallic substrate	19	21
L2	Metallic reflective layer	0.1	0.3
L3	Optical interference layer	0.1	0.3
L4	Thermal buffering and optical tuning layer	1.5	3.5
L5	Antistatic layer	0.02	0.2

The thickness optimization surrogate model is constructed using a fully connected

feedforward neural network architecture with three hidden layers. The input layer accepts the 5-dimensional feature vector, followed by three hidden layers comprising 48, 24, and 12 neurons, respectively, and a 1-dimensional output layer. All hidden layers employ the ReLU activation function. To eliminate scale discrepancies and enhance training stability, both input feature variables and target labels are scaled into the interval [0, 1] via min-max normalization according to Eq. (24):

$$x_{\text{norm}} = \frac{x - x_{\min}}{x_{\max} - x_{\min}} \tag{24}$$

The fully connected network architecture of the thickness optimization surrogate model is illustrated in Fig. 8.

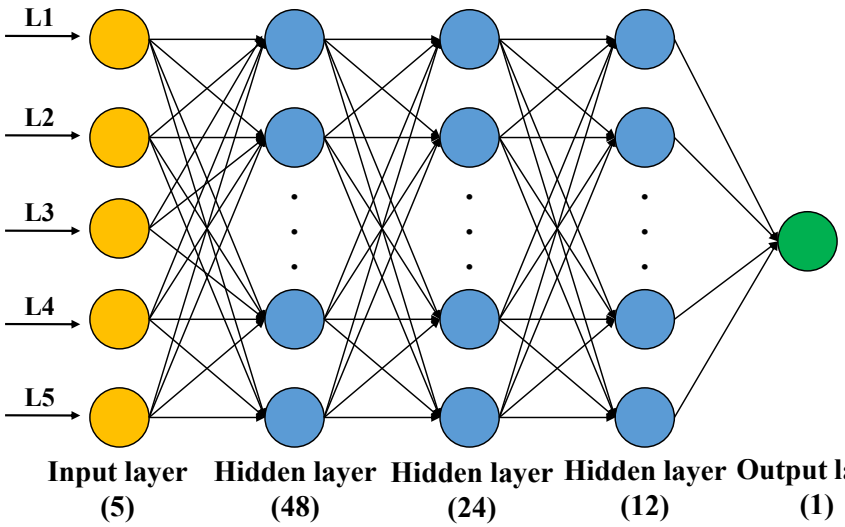


Fig. 8 Network architecture of the BP neural network surrogate model for continuous thickness optimization

3.2.2 Model Training and Performance Evaluation

The training of the thickness surrogate network is executed using the Adam optimizer with an initial learning rate of 10^{-3}, a weight decay coefficient of 10^{-4}, and a maximum budget of 500 training epochs, employing Mean Squared Error (MSE) as the loss function. The training loss trajectory is depicted in Fig. 9, demonstrating smooth and stable convergence across training epochs.

The predictive accuracy of the surrogate model on the test dataset is quantitatively evaluated using the coefficient of determination (R^2) and the Root Mean Squared Error (*RMSE*), defined as follows:

$$R^2 = 1 - \frac{\sum_{i=1}^{n}(T_i - \hat{T}_i)^2}{\sum_{i=1}^{n}(T_i - \bar{T})^2} \tag{25}$$

$$RMSE = \sqrt{\frac{1}{n}\sum_{i=1}^{n}(T_i - \hat{T}_i)^2} \tag{26}$$

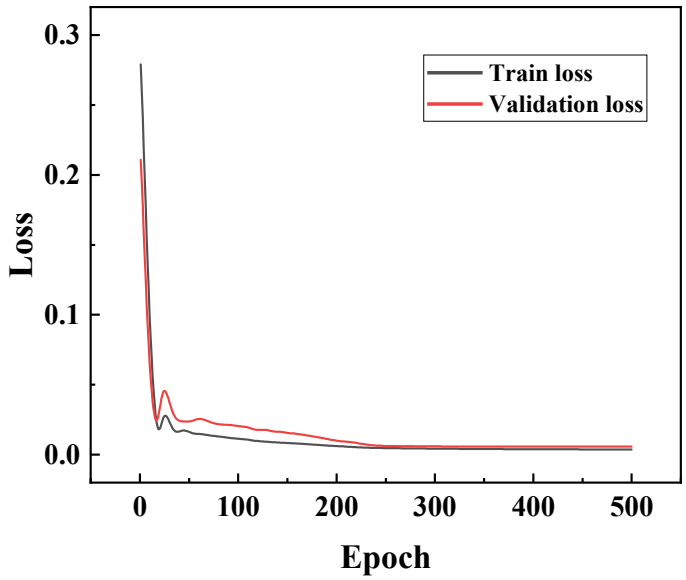


Fig. 9 Training and validation loss curves of the thickness optimization surrogate model

The trained surrogate model achieves an R^2 of 0.87 and an *RMSE* of 26.08K on the test set. Fig. 10 presents the scatter plot comparing the predicted peak temperatures against the full finite element simulation outputs. The data points are concentrated closely along the 1:1 ideal reference line (y=x), confirming that the constructed surrogate model reliably captures the complex nonlinear mapping between functional layer thicknesses and peak transient temperatures.

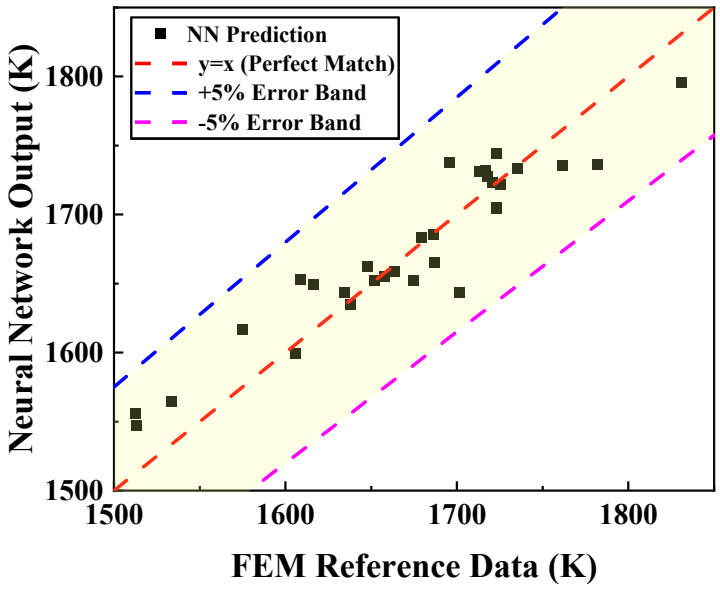


Fig. 10 Scatter plot comparing the surrogate model predictions with the finite element simulation results

3.2.3 Thickness Combination Optimization

Utilizing the trained BP neural network surrogate model, the NSGA-II is deployed to perform global optimization across the continuous thickness design space. The primary objective is to minimize the predicted peak transient temperature:

$$\min_{\mathbf{L}} T_{peak} = f_{BP}(\mathbf{L}) \tag{27}$$

subject to the design space constraints:

$$L_i^{\min} \le L_i \le L_i^{\max}, \quad \sum_{i=1}^{5} L_i \le 25\ \mu m \tag{28}$$

The NSGA-II parameters are configured with a population size of 120, a maximum generation budget of 400, a crossover probability of 0.9, and a mutation probability of 0.2. To handle constraint satisfaction during evolutionary search, a dynamic penalty function method is incorporated to penalize candidates violating thickness bounds, ensuring that the population evolves consistently toward the feasible design space. Finally, the optimal thickness configuration selected by NSGA-II is re-evaluated within the high-fidelity finite element framework to establish a closed-loop validation, confirming the predictive reliability of the surrogate model. Detailed optimization results and comparative analyses are elaborated in Section 4.3.

4. Results and Discussion

4.1 Material Combination Screening Results

Utilizing the trained BP neural network surrogate model, the GA executed a global search across the discrete five-layer material combination space, yielding a total of 20 feasible candidate configurations. Among these, the top five optimal material candidate combinations ranked by the lowest predicted peak transient temperature are summarized in Table 5.

Table 5 Top five optimal material candidate combinations identified by Stage 1 screening

Rank	L1	L2	L3	L4	L5
1	SUS304	Ag	Si_3N_4	SiO_2	ITO
2	SUS304	Ag	Si_3N_4	SiO_2	AZO
3	SUS304	Ag	Si_3N_4	SiO_2	TTO
4	TC4	Ag	Si_3N_4	SiO_2	ITO
5	SUS304	Ag	Si_3N_4	SiO_2	AZO

Following the stage 1 material screening, the optimal material candidate configuration obtained is SUS304/Ag/Si_3N_4/SiO_2/ITO. Full-field finite element verification of this optimized stack yielded a peak transient temperature of 1673.6 K, representing a significant thermal reduction of 49.4 K compared to the baseline architecture and successfully maintaining the structural response below the critical phase-change threshold.

4.2 Refined Thickness Optimization Results

With the optimal material combination screened in the first stage as a fixed configuration, the NSGA-II algorithm is executed to perform global search optimization over the continuous five-layer thickness design space.

The optimal thickness combination identified by NSGA-II is summarized in Table 6. The peak temperature predicted by the surrogate model is 1543.6 K. To confirm the predictive accuracy and reliability of the optimization, this optimal thickness configuration is re-evaluated in the optical–thermal–ablation coupled finite element

model for validation. The simulation yields an actual peak temperature of 1513.4 K, exhibiting a low relative error of 1.96% compared with the surrogate model prediction. This excellent agreement confirms that the constructed surrogate model possesses high fidelity in the vicinity of the global optimum. Consequently, the two-stage optimized thin-film architecture successfully achieves a cumulative thermal reduction of 209.6 K relative to the initial baseline structure.

Table 6 Comparison of thickness optimization.

Layer position	Material	Initial thickness (μm)	Optimal thickness (μm)
L1	SUS304	20.5	21
L2	Ag	0.15	0.106
L3	Si_3N_4	0.15	0.18
L4	SiO_2	2.6	2.35
L5	ITO	0.02	0.05

4.3 Discussion

4.3.1 Thermal Management Mechanisms of Material Combination Optimization

Fig. 11(a) compares the peak transient surface temperatures across metallic substrate candidates. Under identical thermal loads, TC4 and Invar alloy yield peak temperatures 35.75 K and 9.88 K higher than SUS304, respectively. This performance stems from two coupled thermal attributes: a higher thermal conductivity that facilitates rapid lateral and inward heat diffusion, and a positive temperature coefficient of thermal conductivity over 300 to 1800 K. As high-power irradiation elevates local temperatures, the thermal transport capability of SUS304 dynamically increases, boosting heat dissipation. Conversely, TC4 and Invar exhibit low thermal conductivities with negligible temperature responsiveness, leading to severe localized heat entrapment.

Fig. 11(b) illustrates the peak thermal response of reflective layers. The peak temperature follows the sequence Ag<Au<Al, inversely matching their optical reflectivities at 1064 nm (Ag>Au>Al). This underscores optical absorptivity as the dominant governor of initial heat deposition. Although peak temperatures across all candidates exceed their respective melting thresholds, Ag demonstrates a decisive advantage in delaying failure onset due to its minimal heat deposition combined with a high phase-change threshold. Although Au possesses a higher melting point, its lower reflectivity increases energy absorption and elevates the peak temperature by nearly 150 K, offsetting its thermal margin. Al, suffering from both the lowest reflectivity and melting point, exhibits accelerated heating and premature thermal damage.

For the optical interference layer, Si_3N_4 exhibits superior performance over alternative ceramics like Al_2O_3, as shown in Fig. 11(c). At 1064 nm, the optical extinction coefficient of Si_3N_4 is roughly one-tenth that of Al_2O_3, directly scaling down volumetric heat generation and lowering the peak transient temperature by 49.4 K. Thermally, both ceramics fall into the low-conductivity regime (0.7 W/(m·K) for Si_3N_4 and 1.73 W/(m·K) for Al_2O_3). Sensitivity analysis indicates that this 2.5 times thermal conductivity variance exerts a negligible effect compared to the order-of-magnitude difference in optical absorption. Thus, optical absorption mitigation serves as the primary driver for thermal reduction, with passive conduction playing only a secondary

role.

Among antistatic layers, ITO displays thermal performance closely matching AZO and TTO, with peak temperature variations within 6 K, as shown in Fig. 11(d). This limited sensitivity arises from the nanoscale thickness and minimal optical absorption at 1064 nm across all three conductors. Given their equivalent opto-thermal impacts, material selection defaults to process maturity and deposition stability, where ITO remains the optimal industrial choice.

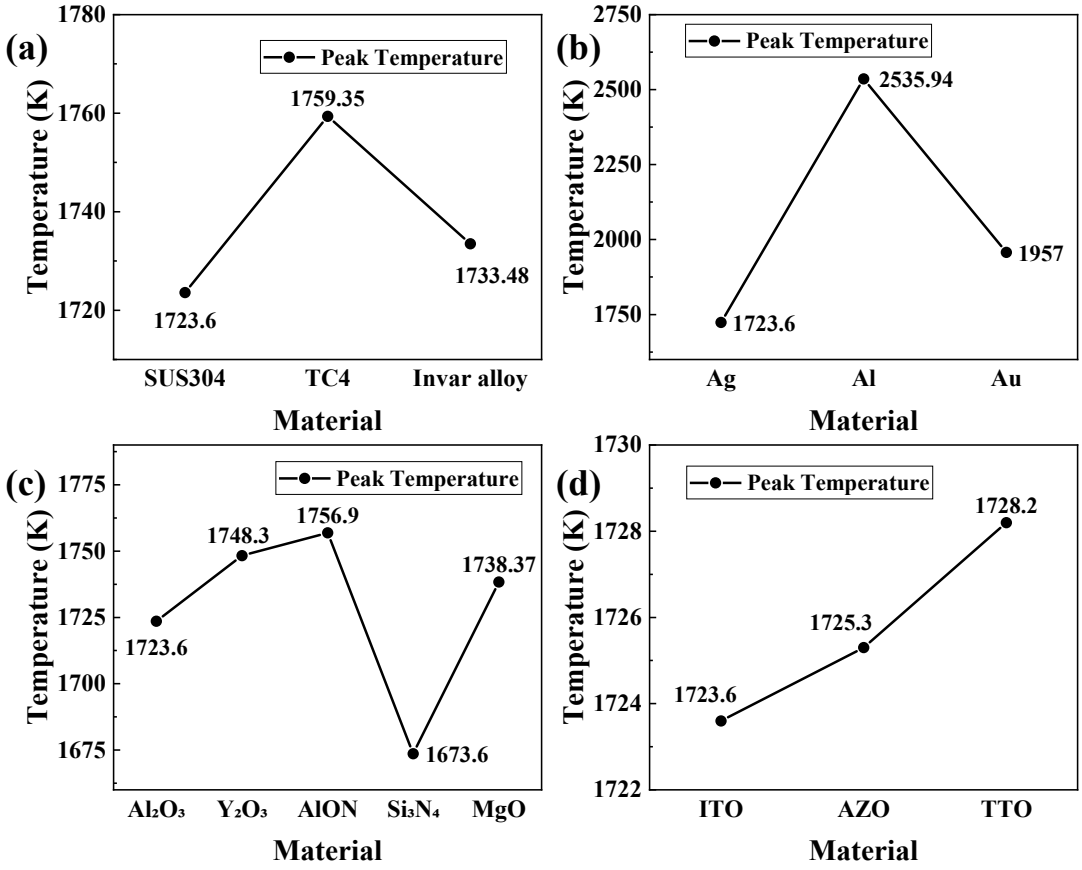


Fig. 11 Comparison of peak transient temperatures across candidate material combinations: (a) metallic substrate materials; (b) metallic reflective layer materials; (c) optical interference layer materials; (d) antistatic layer materials

4.3.2 Sensitivity Analysis of Layer Thickness Optimization

Fig. 12(a) presents the peak transient temperature of the thin-film architecture as a function of SUS304 substrate thickness. The primary role of substrate is modulating the passive heat-sink capacity by scaling the thermal diffusion volume. Adjusting substrate thickness from 20.5 μm to 21 μm provides additional thermal dissipation volume under the total thickness constraint, achieving a 2.4 % reduction in peak temperature.

The sensitive temperature trajectory with respect to the reflective layer thickness is depicted in Fig. 12(b). As Ag thickness increases from 0.106 μm to 0.2 μm, the peak temperature climbs by 40 K, dominated by elevated cross-plane thermal resistance toward the substrate. Beyond 0.2 μm, however, further thickening enhances in-plane heat spreading while shifting the standing-wave absorption peak away from high-loss interfacial regions, which halts further thermal escalation. This non-monotonic

behavior underscores the competition between cross-plane thermal resistance and in-plane thermal mitigation coupled with optical absorption distribution.

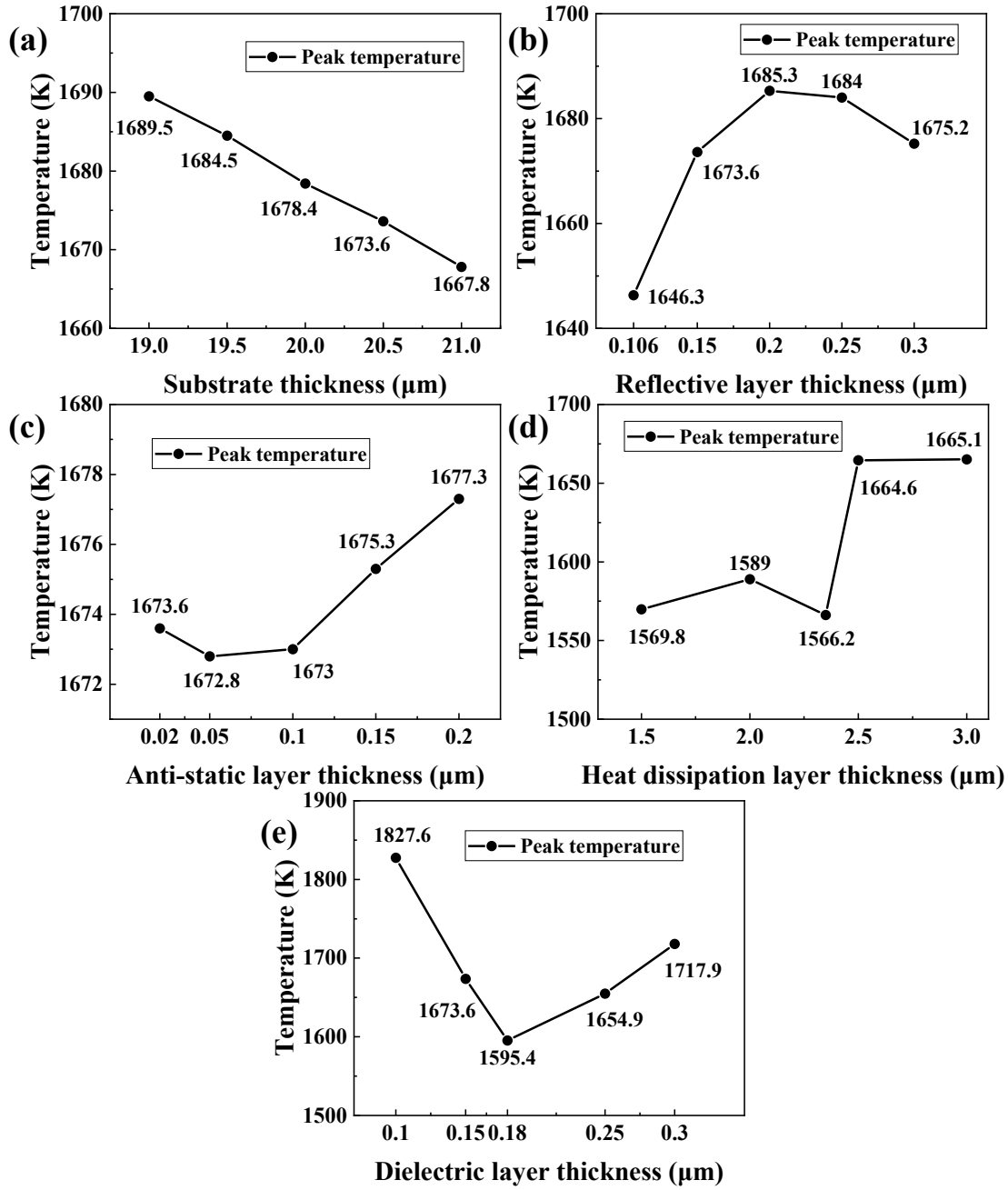


Fig. 12 Sensitivity of peak transient temperature to individual layer thicknesses: (a) substrate; (b) reflective layer; (c) optical interference layer; (d) thermal buffering and optical layer; (e) antistatic layer

Fig. 12(c) illustrates the relationship between the optical interference layer thickness and peak transient temperature. The parabolic response reflects a delicate trade-off: while thickening optical interference layer thickness increases the transverse heat transfer area away from localized hot spots, excessive expansion under a fixed total thickness constraint compresses the SUS304 substrate's heat-sink volume, ultimately impairing bottom-side thermal dissipation.

As shown in Fig. 12(d), the impact of the thermal buffering and optical layer is

governed by the interplay between optical interference phase shifting and bulk heat accumulation. The temperature drop observed between 2 and 2.35 μm stems from favorable interference conditions that suppress absorption in the underlying Ag layer. Conversely, the sharp 98.4 K temperature jump near 2.5 μm marks an interference phase transition that intensifies the local electric field within the reflective interface. Beyond 2.5 μm, optical absorption reaches saturation, balancing the effects of increased cross-plane thermal resistance and volumetric heat capacity.

As shown in Fig. 12(e), the antistatic layer exerts a secondary influence on macro-thermal response. In the ultrathin regime, optimizing ITO thickness enhances optical impedance matching with the underlying SiO_2 layer, slightly lowering peak temperatures. Above 0.05 μm progressive parasitic optical absorption within the ITO bulk leads to a monotonic temperature rise.

5. Conclusions

(1) A coupled wave-optical and high-temperature transient thermal model was established by integrating Helmholtz wave optics with temperature-dependent transient Fourier heat conduction, wherein the enthalpy-based equivalent heat capacity method captured solid–liquid phase transitions. Validated against damage threshold experiments under seven distinct laser power levels, the simulated thermal damage states agreed closely with experimental observations, demonstrating high fidelity in capturing the transient thermal evolution and layer-by-layer melting behavior of multilayer thin films under continuous-wave laser irradiation.

(2) A two-stage decoupled opto-thermal optimization framework was developed to separate discrete material selection from continuous thickness design. By utilizing BP neural network surrogate models to substitute high-fidelity finite element evaluations within the Genetic Algorithm and NSGA-II workflows, computational expenditure across the high-dimensional mixed-variable space was substantially reduced without compromising predictive accuracy.

(3) Global screening across 15 candidate material configurations identified SUS304/Ag/Si_3N_4/SiO_2/ITO as the optimal material architecture. Finite element validation yielded a peak surface temperature of 1673.6 K, representing a 49.4 K reduction relative to the baseline structure. Mechanistic analysis revealed that suppressing optical absorption via an order-of-magnitude reduction in the optical extinction coefficient serves as the primary driver for thermal mitigation, vastly outstripping the influence of intrinsic thermal conductivity. Furthermore, the positive temperature coefficient of thermal conductivity in the SUS304 substrate provides a dynamic heat dissipation boost under localized high-temperature conditions.

(4) Multi-objective thickness optimization conducted under a 25 μm total thickness budget established the refined optimal configuration: SUS304 substrate (21 μm)/Ag (0.106 μm)/Si_3N_4 (0.18 μm)/SiO_2 (2.35 μm)/ITO (0.05 μm). Full-field simulation confirmed a peak transient temperature of 1513.4 K, achieving a cumulative thermal reduction of 209.6 K (12.2%) compared with the initial baseline. Crucially, the thermal impact of layer thicknesses exhibited distinct non-monotonic features governed by competing mechanisms. Specifically, the thermal response to Ag layer thickness is governed by the trade-off between cross-plane thermal resistance escalation and in-

plane thermal spreading coupled with absorption peak shifting. Meanwhile, the SiO_2 layer thickness dictates thermal accumulation through the synergy of bulk optical energy dissipation and interference standing-wave phase modulation.

Declarations

CRediT authorship contribution statement

Yuyang Shen: Data curation, Formal analysis, Investigation, Visualization, Writing - original draft. Shu Zheng: Conceptualization, Project administration, Writing - review & editing. Duanpeng He: Software, Resources, Validation. Yang Cui: Visualization. Yan Li: Funding acquisition, Supervision. Yuxiong Xue: Methodology, Resources, Supervision.

Competing interests

The authors have no competing interests to declare that are relevant to the content of this article.

Data Availability Statement

Data are available upon reasonable request and with permission from all authors.

Funding

This work was supported by the Postgraduate Research and Practice Innovation Program of Jiangsu Province (No. 26CXJH6771).

Acknowledgements

Not applicable.

References

[1] Soulier M, Rapaport A, Krol H, et al. Measurement and simulation of wavefront deformation induced by a high-power CW laser in thin-film optical filters. Applied Optics, 2026, 65(5): A68-A78.

[2] Haque S M, De R, Prathap C, et al. CW laser damage study in Ag/TiO_2 bilayer thin films: Role of interfacially diffused plasmonic silver nanoparticles. Optical Materials, 2021, 117: 111135.

[3] Xue W, Zhang Z, Dou P, et al. Thermodynamic mechanism in colored glass substrates of interference filters under continuous-wave laser irradiation. Scientific Reports, 2025, 15: 34438.

[4] Taylor L N, Brown A K, Pung A J, et al. Continuous-wave laser damage of uniform and nanolaminate hafnia and titania optical coatings. Optics Letters, 2013, 38(21): 4292-4295.

[5] Xu J, Chen J, Chen P, et al. Continuous-wave laser damage mechanism of a spectral combining grating. Applied Optics, 2019, 58(10): 2551-2555.

[6] Kim I, So S, Mun J, et al. Optical characterizations and thermal analyses of HfO_2/SiO_2 multilayered diffraction gratings for high-power continuous wave laser. Journal of Physics: Photonics, 2020, 2(2): 025004.

[7] Zhang Y, Castelli Astrath NG, Lukasievicz GVB, et al. Understanding and designing photothermal responses in complex layered systems. Scientific Reports, 2025, 15: 26173.

[8] Bovard B G, Macleod H A. Nonlinear behaviour of optical coatings subjected to

intense laser irradiation. Journal of Modern Optics, 1988, 35(7): 1151-1168.
[9] Moorhead M S, Avedisian C T. Heat transfer in multilayered thin film materials applied to photothermal deflection spectroscopy. Journal of Thermophysics and Heat Transfer, 2021, 35(4): 1-12.
[10] Grigoriev F V, Sulimov V B, Tikhonravov A V. High-performance modeling of laser induced heating of TiO_2-SiO_2 thin films. Lobachevskii Journal of Mathematics, 2025, 46(8): 3678-3686.
[11] Yamada M. Temperature distributions produced in multilayer structures by a scanning CW laser beam. Japanese Journal of Applied Physics, 1991, 30(7): 1418-1427.
[12] Braun J L, Hopkins P E. Upper limit to the thermal penetration depth during modulated heating of multilayer thin films with pulsed and continuous wave lasers. Journal of Applied Physics, 2017, 121: 175107.
[13] Ahmmed M S, Huda N. Modelling laser-induced heat transfer phenomena of thin-films using OpenFOAM. Applied Mathematical Modelling, 2019, 71: 394-407.
[14] Zhang J, Song J, Chen H, et al. A thermal physics model of continuous wave laser irradiation of SiO_2/Ge/sapphire epitaxial films. Science of Advanced Materials, 2018, 10(10): 1457-1465.
[15] Gallais L, Commandré M. Photothermal deflection in multilayer coatings: modeling and experiment. Applied Optics, 2005, 44(24): 5230-5237.
[16] Ocak M, Sert C, Okutucu-Özyurt T. Effects of optical design modifications on thermal performance of a highly reflective HfO_2/SiO_2/TiO_2 three material coating. Heat and Mass Transfer, 2018, 54(2): 377-384.
[17] Voller V R, Prakash C. A fixed grid numerical modelling methodology for convection-diffusion mushy region phase-change problems. International Journal of Heat and Mass Transfer, 1987, 30(8): 1709-1719.
[18] Nedjar B. An enthalpy-based finite element method for nonlinear heat problems involving phase change. Computers & Structures, 2002, 80(1): 9-21.
[19] Kopp P, Calo V, Rank E, et al. Space-time hp-finite elements for heat evolution in laser powder bed fusion additive manufacturing. Engineering with Computers, 2022, 38(6): 4879-4893.
[20] Brent A D, Voller V R, Reid K J. Enthalpy-porosity technique for modeling convection in solidifying systems. Numerical Heat Transfer, 1988, 13(3): 297-318.
[21] Resl J, Hingerl K, Gutierrez Y, et al. Optimizing laser-induced phase transformations in Sb_2S_3 thin films: Simulation framework and experiments. Journal of Applied Physics, 2024, 136(17): 1-16.
[22] He M, Zhigilei L V. Multiscale modeling of short pulse laser induced amorphization of silicon. Journal of Applied Physics, 2024, 136(21): 213103.
[23] Malkiel I, Mrejen M, Nagler A, et al. Plasmonic nanostructure design and characterization via Deep Learning. Light: Science & Applications, 2018, 7(1): 60.
[24] Peurifoy J, Shen Y, Jing L, et al. Nanophotonic particle simulation and inverse design using artificial neural networks. Science Advances, 2018, 4(6): eaar4206.
[25] Alkhazraji E, Mukhtar S, Khaled H, et al. AI-driven optimization of multilayer thin-film structures for advanced optical applications. IEEE Access, 2025, 13:

128173-128183.
[26] Deb K, Pratap A, Agarwal S, et al. A fast and elitist multiobjective genetic algorithm: NSGA-II. IEEE Transactions on Evolutionary Computation, 2002, 6(2): 182-197.
[27] Unni R, Yao K, Han X, et al. A mixture-density-based tandem optimization network for on-demand inverse design of thin-film high reflectors. Nanophotonics, 2021, 10(16): 4057-4065.
[28] Zhao Q, Fan Z X, Wang Z J. Role of interface absorption in laser-induced local heating of optical coatings. Optical Engineering, 1997, 36(5): 1530-1536.
[29] McKay M D, Beckman R J, Conover W J. A comparison of three methods for selecting values of input variables in the analysis of output from a computer code. Technometrics, 1979, 21(2): 239-245.